JGR Space Physics

RESEARCH ARTICLE
10.1029/2021JA029712

Energy Budgets From Collisionless Magnetic Reconnection Site to Reconnection Front

Yukang Shu[1], San Lu[2,3], Quanming Lu[2,3], Weixing Ding[1], and Shui Wang[2,3]

[1]School of Nuclear Science and Technology, University of Science and Technology of China, Hefei, China, [2]School of Earth and Space Sciences, CAS Key Laboratory of Geospace Environment, University of Science and Technology of China, Hefei, China, [3]CAS Center for Excellence in Comparative Planetology, Hefei, China

Key Points:

- Energy budgets from collisionless magnetic reconnection site to reconnection fronts are studied through two-dimensional particle-in-cell simulations
- The reconnection fronts that dominate the energy conversion are generated from the reconnection site
- Energy conversion at the well-developed reconnection front is unrelated to the reconnection site. The Poynting flux inflow is mainly converted to enthalpy flux

Correspondence to:
S. Lu and Q. Lu,
lusan@ustc.edu.cn;
qmlu@ustc.edu.cn

Citation:
Shu, Y., Lu, S., Lu, Q., Ding, W., & Wang, S. (2021). Energy budgets from collisionless magnetic reconnection site to reconnection front. *Journal of Geophysical Research: Space Physics*, *126*, e2021JA029712. https://doi.org/10.1029/2021JA029712

Received 24 JUN 2021
Accepted 23 SEP 2021

Abstract Collisionless magnetic reconnection occurs ubiquitously in space plasma environments and plays an important role in energy conversion therein. In collisionless magnetic reconnection, the reconnection site is usually unsteady and ejects reconnection fronts away from it. Using two-dimensional particle-in-cell simulations, we study the energy budgets from the collisionless magnetic reconnection site to reconnection fronts. It is concluded that the reconnection rate cannot well reflect energy conversion of nonsteady state magnetic reconnection because energy conversion occurs predominantly at the reconnection fronts, whereas the reconnection rate can only represent the energy conversion at the reconnection site. We clarify the connection between the reconnection site and the reconnection fronts in terms of energy conversion. The reconnection site functions as a trigger and energy source that generates the outflow of Poynting flux, bulk kinetic energy flux, and enthalpy flux forming the reconnection fronts that move downstream. The well-developed reconnection fronts are no longer related to the reconnection site. The energy income at the reconnection fronts is mainly the Poynting flux from their top and bottom boundaries, most of which is transformed to $\overline{\mathbf{P}} \cdot \mathbf{V}$ flux flowing downstream out of the moving front through the work by the electric field. The work done by the electric force is compensated with the work done by the thermal pressure gradient, which guarantees that the released magnetic energy is mostly converted to thermal energy.

1. Introduction

Magnetic reconnection is a process of energy conversion from magnetic field to plasmas. During magnetic reconnection, topologies of magnetic fields change and magnetic energy is released to particle heating and acceleration (Birn & Priest, 2007; Yamada et al., 2010). It provides explanations for many explosive phenomena in space plasmas, such as solar flares (Masuda et al., 1994), coronal mass ejections (Lin & Forbes, 2000), and geomagnetic substorms (Baker et al., 1996; Kepko et al., 2015). Laboratory experiments have also reported occurrences of magnetic reconnection (Yamada et al., 1994).

One key question for magnetic reconnection is the energy conversion. Birn and Hesse (2005, 2010) studied the energy budgets in magnetic reconnection using MHD and localized particle-in-cell simulations. They concluded that the Poynting flux from the tail lobe is converted to thermal energy through bulk kinetic energy as a mediator. Using hybrid simulations, Aunai et al. (2011) discovered that ions are inclined to gain thermal energy instead of kinetic energy. Q. Lu, Lu, Huang, Wu, and Wang (2013) and S. Lu, Lu, Huang, and Wang (2013) used two-dimensional (2D) particle-in-cell (PIC) simulations to study the energy conversion of electrons near the reconnection site and in the magnetic island and found that electrons are heated and form the enthalpy flux flowing toward the magnetic island. Eastwood et al. (2013) also verified that the ion enthalpy flux is dominant in the partition of energy flux through satellite observations. Experiments on energy conversion in magnetic reconnection have also been carried out (Yamada et al., 2014, 2015). They found that half of the magnetic energy is converted to particles, 2/3 of which is given to ions, and 1/3 to electrons.

However, when zoomed out from the reconnection region to the global-scale phenomena, such as geomagnetic substorms, it has been found by Angelopoulos et al. (2013) that the energy conversion during substorms predominantly occurs at reconnection fronts, whereas the energy conversion at reconnection site itself is much less. Using PIC simulations, Goldman et al. (2015) also showed that energy conversion

(especially ions) predominantly occurs at the reconnection fronts in comparison with the reconnection site. Yi et al. (2019) found that the energy conversion rate peaks later than the reconnection rate and also concluded that the energy conversion primarily happens at the reconnection fronts. In addition, Shay et al. (2014) investigated the electron heating during magnetic reconnection through simulation; their study indicates that the energy partition may not be determined by the reconnection rate. Here, reconnection fronts are magnetic reconnection's ejecta moving away from the reconnection site, which consist of reconnected magnetic flux and plasma outflows. Reconnection fronts are usually referred to as dipolarization fronts and jet fronts as well (Deng et al., 2010; Divin et al., 2015; Huang et al., 2015; C. M. Liu, Fu, Vaivads, et al., 2018; J. Liu et al., 2014; Runov et al., 2009; Sitnov et al., 2009; M. Zhou et al., 2009). Spacecraft observations usually recognize a reconnection front as a sharp increase in B_z component along with a decrease in plasma density (H. S. Fu et al., 2013; C. M. Liu, Fu, Xu, et al., 2018; Wu et al., 2013; Xu et al., 2018). A typical reconnection-forming front mainly comprises downstream Poynting flux and enthalpy flux (Lapenta et al., 2014; S. Lu et al., 2015; Vapirev et al., 2013; Wang et al., 2020; Yao et al., 2017). However, it remains unclear how the energy conversion at reconnection fronts connects to that at reconnection site, especially during the formation of the fronts. Song et al. (2020) investigated the force and energy balance at the developing reconnection front and analyzed how fronts are accelerated and the energy source that heats and accelerates the electrons and ions. Moreover, for the well-developed reconnection fronts, although previous simulations and observations have examined the energy conversion rate $\mathbf{J}\cdot\mathbf{E}$ (Khotyaintsev et al., 2017; Sitnov et al., 2009; Zhong et al., 2019), such examinations do not reveal the entire energy budgets. For example, it remains unclear that what supplies the strong $\mathbf{J}\cdot\mathbf{E}$, how much energy goes to electron/ion heating, bulk flows, and different kinds of energy flow.

Following the above rationale, in this paper, we study the energy budgets from the collisionless magnetic reconnection site to reconnection fronts by using two-dimensional (2D) particle-in-cell (PIC) simulations. We demonstrate why the energy conversion is dominated by the reconnection front rather than the reconnection site. In addition, we focus on the origin and development of energy conversion at the reconnection site and front by studying the connections and differences between them. We describe our simulation setup in Section 2, and the simulation results are presented in Section 3. Discussions and conclusions are given in Section 4.

2. Simulation Setup

We applied a 2D explicit particle-in-cell (PIC) method to perform the simulation. The code has been successfully applied to study magnetic reconnection (X. R. Fu et al., 2006; Huang et al., 2010; Q. Lu et al., 2010). The electric field and magnetic field are defined on grids in the x-z plane and updated by solving Maxwell's equations. The electrons and ions are modeled as macroparticles and advanced in the electromagnetic fields by solving their motion equations. The initial condition is a Harris current sheet with a uniform background plasma. The initial magnetic field is $\mathbf{B} = B_0 \tanh\left(z/\delta\right)\mathbf{e}_x$, where B_0 denotes the asymptotic magnetic field and δ denotes the half-width of the current sheet. Here, we use $\delta = 0.6d_i$, where $d_i \equiv c/\omega_i$ denotes the ion inertial length and $\omega_{\rm pi} \equiv \sqrt{n_0 e^2/\varepsilon_0 m_i}$ is the ion plasma frequency. We also add a small perturbation on the magnetic field at the center of the simulation domain to expedite the occurrence of magnetic reconnection. The initial density of the plasma is $n = n_0 sech^2 z/\delta + n_b$, where n_0 is the peak density of the Harris current sheet and n_b is the uniform background plasma density. The background density n_b is 20% of n_0. The ion-electron temperature ratio is 4:1. The temperature is uniform and isotropic in the simulation domain.

The size of the 2D simulation box is $L_x \times L_z$, with $L_x = 100d_i$ and $L_z = 10d_i$. The grid spacing is $\Delta x = \Delta z = 0.05d_i = 0.5d_e$, and time step is $\Delta t = 0.001\Omega_i^{-1}$. $d_e \equiv c/\omega_{\rm pe}$ stands for the electron inertial length and $\Omega_i \equiv eB_0/m_i$ is the ion gyrofrequency. The mass ratio between ion and electron is taken as 100 in our simulation. The speed of light is taken as $c = 15v_A$, where $v_A \equiv B_0/\sqrt{\mu_0 m_i n_0}$ is the Alfvén velocity. We put 4×10^7 particles in total in the simulation. Periodic boundary conditions are applied in the x-direction, and perfect conductor boundary conditions are applied in the z-direction.

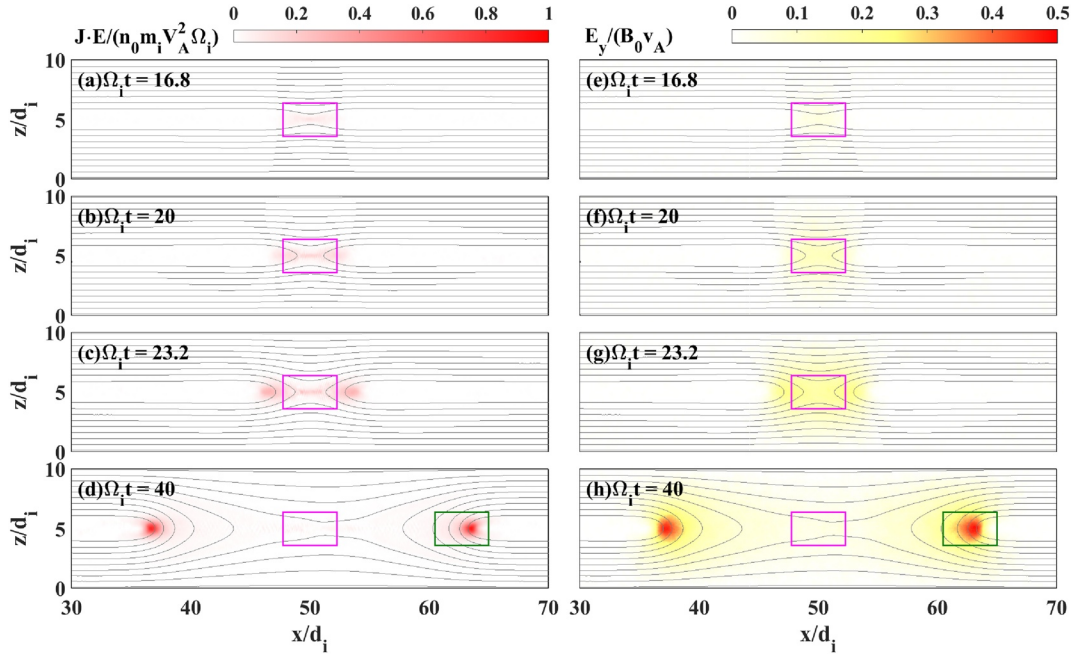

Figure 1. Overview of the work $\mathbf{J} \cdot \mathbf{E}$ (left) and y component of the electric field E_y (right) with magnetic field lines (black lines) at $\Omega_i t$ =16.8, 20.0, 23.2, and 40.0.

3. Results

3.1. Overview

Figure 1 gives an overview of the magnetic reconnection process. Work by electric field $\mathbf{J} \cdot \mathbf{E}$ (left column) and the electric field component E_y (right column) is presented. Positive work by electric field indicates that the magnetic energy is dissipated and converted to the plasma. Starting from the reconnection site at $t = 16.8\Omega_i^{-1}$, energy conversion grows with the reconnection electric field due to collisionless tearing instability. Fronts emerge at two flanks of the reconnection site since $t \sim 20.0\Omega_i^{-1}$. As fronts develop and move downstream, they gradually dominate the energy conversion in the whole reconnection process. This is consistent with previous simulations by Q. Lu, Lu, Huang, Wu, and Wang (2013) and S. Lu, Lu, Huang, and Wang (2013), which found that the growth rate of the electric field E_y at the pileup region is about twice that at the reconnection site (Q. Lu, Lu, Huang, Wu, & Wang, 2013). After formation, fronts gain a steady moving speed downstream, and the energy conversion at fronts reaches a dynamic balance, which will be discussed in detail below.

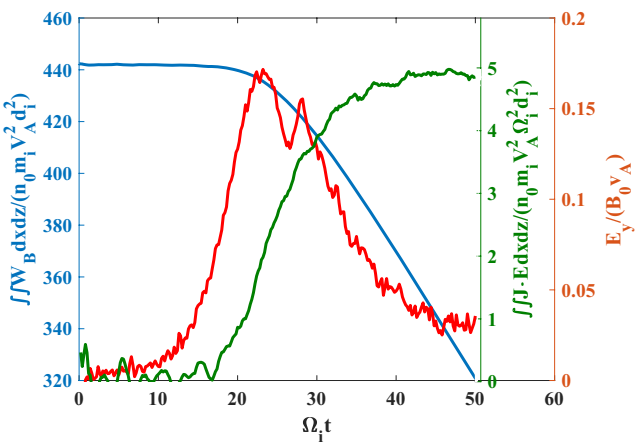

Figure 2. Evolution of total magnetic energy (blue), reconnection rate (red), and integrated work over the whole region, that is, energy conversion rate (green).

It should be clear that both the reconnection site and fronts are inevitable in researching energy conversion, which will be presented in Sections 3.2 and 3.3, respectively. To elucidate the relation between the reconnection site and fronts, the formation of the reconnection fronts near the reconnection site is investigated in Section 3.3. To better quantify the energy budgets, two boxes of the same size are set to mark two major energy converting sites: the reconnection site (pink) and the right-side reconnection front (green). Because the reconnection site stays at the center of the simulation domain, the pink box is chosen to be static at the reconnection site. The reconnection fronts move once they are well developed, so the green box at the right-side reconnection front moves along with it. The situation at the left-side front is similar due to symmetry.

Figure 2 shows the time evolution of total magnetic energy, reconnection rate, and $\iint \mathbf{J} \cdot \mathbf{E}\, dxdz$. All these terms are normalized. The

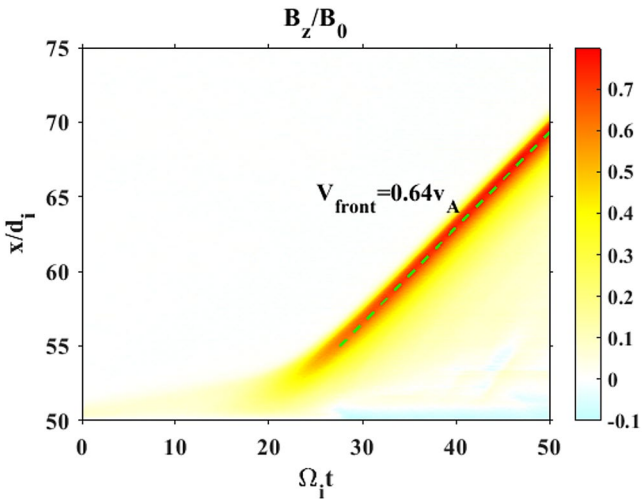

Figure 3. B_z component on right x-axis over time. The moving front is outstanding comparing with the background. During $t = 27.6\Omega_i^{-1} - 50.0\Omega_i^{-1}$, the moving speed can be approximated as constant about $0.64v_A$ (green dashed line).

reconnection rate is defined as the y-component of the electric field at the reconnection site, normalized by asymptotic magnetic field B_0 and the characteristic Alfvén velocity. The reconnection rate is always applied to represent the rate that the reconnection proceeds in the steady-state reconnection. According to the field energy conversion equation, $\partial\left(\varepsilon_0 E^2 + B^2/\mu_0\right)/\partial t + \nabla \cdot \mathbf{S} = -\mathbf{J} \cdot \mathbf{E}$ (electric field energy is negligible). The decreasing rate of magnetic energy of the system can be expressed as work integrated over the whole region, $\iint \mathbf{J} \cdot \mathbf{E}\, dxdz$ (2D simulation, integrated in the x-z plane), namely energy conversion rate, since Poynting flux at boundaries can be neglected. As shown in the figure, the energy conversion rate and the reconnection rate peak asynchronously. The maximum reconnection rate is 0.17 at $t = 23.2\Omega_i^{-1}$. At this time, magnetic energy declines merely 1.5%. Nevertheless, the energy conversion rate starts increasing since $t = 16.8\Omega_i^{-1}$ and reaches a plateau at $t = 37.0\Omega_i^{-1}$. The magnetic energy declines at a uniform pace afterward. About 27.5% of the whole magnetic energy is converted to plasmas for the duration of the calculation ($t = 50\Omega_i^{-1}$ in total), which indicates that most of the energy conversion does not take place near the X-line. This is because the main proportion of work is done at fronts instead as shown in Figure 1d. Unlike steady-state reconnection, the reconnection rate in nonsteady state reconnection is an insufficient indication for energy conversion. There exists a small peak at $t = 28.2\Omega_i^{-1}$ following the acme of the reconnection rate. It is attributed to a small magnetic island formed by the secondary reconnection, which does not affect the whole energy conversion.

The time evolution of the reconnected magnetic field (i.e., B_z component at $z = 0$) is shown in Figure 3. The right-side moving front emerges in the diffusion region at the beginning of reconnection and reaches a steady speed at $t = 27.6\Omega_i^{-1}$. It maintains the constant moving speed ($\sim 0.64v_A$) and propagates downstream afterward. Therefore, the green box we choose also moves at a speed of $0.64v_A$. Note that the B_z magnitude also keeps unchanged after $t = 27.6\Omega_i^{-1}$.

Figure 4 explains why the energy conversion at reconnection fronts exceeds that at the reconnection site. The first reason is that the energy conversion rate $\iint \mathbf{J} \cdot \mathbf{E}\, dxdz$ at reconnection front is several times larger than that at the reconnection site. The second reason is that the energy conversion at fronts persists as they propagate downstream and maintains at a high level, whereas the energy conversion at the reconnection site is transient.

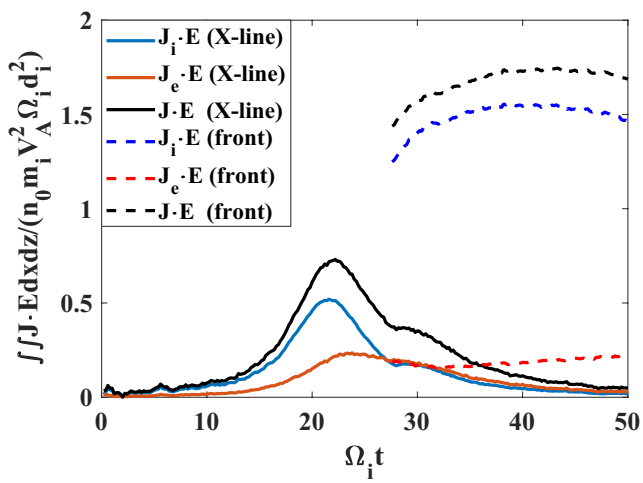

Figure 4. Work by the electric field on electrons, ions, and plasmas at the reconnection site and the front (integrated over boxes at both places, respectively, see Figure 1). Solid lines represent the work at the reconnection site and dashed lines for the front.

$\iint \mathbf{J}_i \cdot \mathbf{E}\, dxdz$ is several times larger than $\iint \mathbf{J}_e \cdot \mathbf{E}\, dxdz$ at the reconnection site (until $t = 27\Omega_i^{-1}$) and at the reconnection front, which indicates that the energy conversion is mainly attributed to ions. This is consistent with previous spacecraft observational results (Khotyaintsev et al., 2017; Zhong et al., 2019). We found that $\iint \mathbf{J}_i \cdot \mathbf{E}\, dxdz$ and $\iint \mathbf{J}_e \cdot \mathbf{E}\, dxdz$ are mainly dominated y-components, that is, $\iint J_y E_y\, dxdz$. The in-plane electric field does not contribute much to the energy conversion. Upon a closer examination, the electric field E_y grows exponentially at the front. The ion current density remains the same level as the unreconnected current sheet. However, the electric current density happens to descend. The ions are unmagnetized, while the electrons are magnetized at the reconnection front, which makes ions easier to gain energy from the electric field than electrons. As a result, the ratio between the energy conversion to ions and electrons increases from 2:1 at the reconnection site to 6:1 at the reconnection front.

The energy conversion equations can be written as follows:

$$\partial W_E/\partial t + \partial W_B/\partial t + \nabla \cdot \mathbf{S} = -\mathbf{J} \cdot \mathbf{E} = -\mathbf{J} \cdot \mathbf{E}' + \mathbf{J} \cdot \mathbf{V}_e \times \mathbf{B}, \quad (1)$$

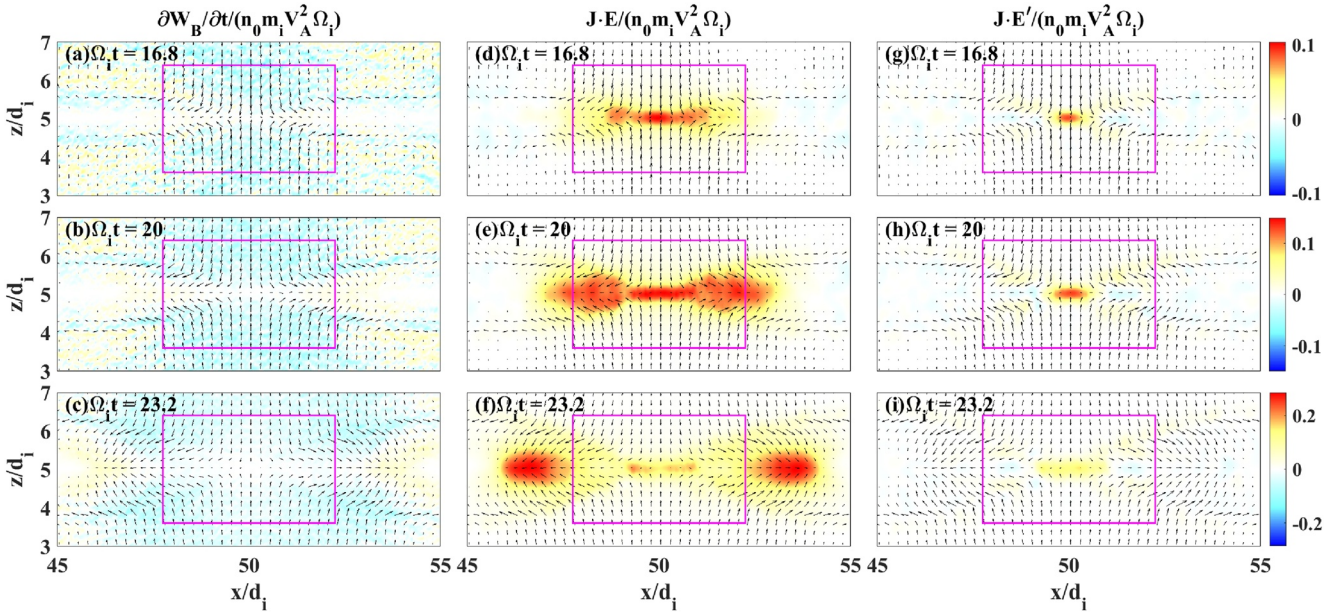

Figure 5. (a–c) Change rate of magnetic energy density $\partial W_B/\partial t$, (d–f) work by electric field $\mathbf{J}\cdot\mathbf{E}$, and (g–i) $\mathbf{J}\cdot\mathbf{E}'$ (work by electron pressure term and electron inertial term) near the reconnection site, shown in colors, with Poynting flux shown in arrows at $\Omega_i t$ =16.8, 20.0, and 23.2.

$$\partial K_s/\partial t + \nabla\cdot\left(K_s\mathbf{V}_s\right) = -\left(\nabla\cdot\bar{\mathbf{P}}_s\right)\cdot\mathbf{V}_s + \mathbf{J}_s\cdot\mathbf{E}, \tag{2}$$

$$\partial U_s/\partial t + \nabla\cdot\mathbf{H}_s + \nabla\cdot\mathbf{Q}_s = \left(\nabla\cdot\bar{\mathbf{P}}_s\right)\cdot\mathbf{V}_s. \tag{3}$$

Equations 1–3 describe the electromagnetic field energy, kinetic energy, and thermal energy conversion, respectively. In the equations, $s = i, e$, where i represents ions and e represents electrons. $\mathbf{J}$ is the electric current density, $\mathbf{E}$ is the electric field, $\mathbf{B}$ is the magnetic field, $\mathbf{V}_s$ is the bulk velocity, $\bar{\mathbf{P}}_s$ is the pressure tensor, $W_E = \varepsilon_0 E^2/2$ is the electric energy density, $W_B = B^2/2\mu_0$ is the magnetic energy density, $\mathbf{S} = \mathbf{E}\times\mathbf{B}/\mu_0$ is the Poynting vector, $K_s = \frac{1}{2}m_s n_s V_s^2$ is the bulk kinetic energy density, $U_s = \frac{1}{2}m_s\int\left(\mathbf{v}-\mathbf{V}_s\right)^2 f_s\left(\mathbf{v}\right)\mathrm{d}\mathbf{v}$ is the thermal energy density, $\mathbf{H}_s = U_s\mathbf{V}_s + \bar{\mathbf{P}}_s\cdot\mathbf{V}_s$ is the enthalpy flux, and $\mathbf{Q}_s = \frac{1}{2}m_s\int\left(\mathbf{v}-\mathbf{V}_s\right)^2\left(\mathbf{v}-\mathbf{V}_s\right)f_s\left(\mathbf{v}\right)\mathrm{d}\mathbf{v}$ is the heat flux. Based on Equations 1–3, in the following sections, we analyze the energy budgets at the reconnection site and reconnection front.

3.2. Reconnection Site

Reconnection begins at the reconnection site as a result of collisionless tearing mode instability (Q. Lu, Lu, Huang, Wu, & Wang, 2013; S. Lu et al., 2020). We examine Equation 1 at the reconnection site in Figure 5. The Poynting flux flows into the reconnection site in the z-direction, and it flows downstream away from the reconnection site in the x-direction. Figures 5d–5f show that magnetic energy is dissipated and converted into work by the electric field $\mathbf{J}\cdot\mathbf{E}$. The regions where $\mathbf{J}\cdot\mathbf{E} > 0$ are called load regions. Load regions start at the reconnection site, expand to two flanks of the X-line at later times, forming the reconnection fronts, and finally concentrate at the moving reconnection fronts. Figures 5g–5i show that the work done by the nonideal electric field, $\mathbf{J}\cdot\mathbf{E}' = \mathbf{J}\cdot\left(\mathbf{E}+\mathbf{V}_e\times\mathbf{B}\right)$, is also positive but more localized right at the center of the reconnection site. This is comprehensible because the nonideal electric field is nonzero in the electron diffusion region at the center of the reconnection site (e.g., Q. Lu, Lu, Huang, Wu, & Wang, 2013; M. Zhou et al., 2019).

For a more quantitative analysis, we integrate the terms in Equation 1 over the pink box plotted in Figure 5, and the results at four representative times are listed in Table 1. At $\Omega_i t$ =16.8, 20.0, and 23.2, when reconnection begins at the reconnection site, the local magnetic energy is released, $\partial W_B/\partial t < 0$. Also, there is a

Table 1
Integration of the Terms in Equation 1 Over the Pink Box at the Reconnection Site

$\Omega_i t$	$\partial W_B/\partial t$	$\partial W_E/\partial t$	$\nabla \cdot \mathbf{S}$	$\mathbf{J} \cdot \mathbf{E}$	$\mathbf{J} \cdot \mathbf{E}'$
16.8	−0.103	0.001	−0.175	0.280	0.054
20.0	−0.228	0.004	−0.405	0.611	0.111
23.2	−0.298	0.007	−0.399	0.688	0.179
40.0	−0.026	−0.001	−0.082	0.114	0.065

significant net inflow of the Poynting flux, $\nabla \cdot \mathbf{S} < 0$, which indicates that the upstream inflow (i.e., the top and bottom boundaries of the pink box) always exceeds the downstream outflow (i.e., the left and right boundaries of the pink box). The released local magnetic energy and the net inflowing Poynting flux account for about 40% and 60% of the energy conversion, respectively. The released magnetic energy and the net inflowing Poynting flux are converted to the plasma kinetic energy through $\mathbf{J} \cdot \mathbf{E}$. Change of the electric field energy is negligible compared to other terms. The term $\mathbf{J} \cdot \mathbf{E}'$ represents the work done by the nonideal electric field, that is, the work done by the electron pressure gradient term and electron inertial term, which contributes to 20% or so, and the 20% is predominantly confined to the electron diffusion region at the center of the reconnection site as shown in Figures 5g–5i.

Both the inflow of Poynting flux $\nabla \cdot \mathbf{S}$ and local magnetic energy dissipation $\partial W_B/\partial t$ decline at the front-moving phase, for instance, at $\Omega_i t$ =40.0 (the last row in Table 1). The reconnection site is superseded by reconnection fronts as the major energy converting region. The latter will be discussed in Section 3.3.

In principle, as described by Equations 2 and 3, the positive work done by the electric field can accelerate ions and electrons, leading to an increase in the bulk kinetic energy K_s or the thermal energy U_s. Note that there is a term $-\left(\nabla \cdot \overline{\mathbf{P}}_s\right) \cdot \mathbf{V}_s$ in Equations 2 and 3, which determines the energy allocation between the bulk kinetic energy and the thermal energy. For ions, as shown in Figures 6d–6f, $\mathbf{J}_i \cdot \mathbf{E}$ is positive at the reconnection site. However, $\left(\nabla \cdot \overline{\mathbf{P}}_i\right) \cdot \mathbf{V}_i$ is also positive and distributes similarly to $\mathbf{J}_i \cdot \mathbf{E}$. Therefore, these two terms compensate each other, leading to little gain in the bulk kinetic energy. Figures 6a–6c show that the ion bulk kinetic energy does not increase but decreases at the reconnection site ($\partial K_i / \partial t < 0$). Nevertheless, the ion bulk kinetic energy manifests itself as the downstream ion bulk kinetic flux $K_i \mathbf{V}_i$ flowing out of the reconnection site (as shown by the arrows). Figure 7 depicts the electron kinetic energy conversion at the reconnection site. Similar to ions, the two source terms, $\mathbf{J}_e \cdot \mathbf{E}$ and $\left(\nabla \cdot \overline{\mathbf{P}}_e\right) \cdot \mathbf{V}_e$, are both positive and distribute similarly at the reconnection site (Figures 7d–7i) and therefore they compensate each other. As a result, the local-time change rate of the electron bulk kinetic energy is almost zero (Figures 7a–7c). The electron bulk kinetic energy flux $K_e \mathbf{V}_e$ also flows out of the reconnection site, and a proportion of it streams out along the separatrices near the reconnection site.

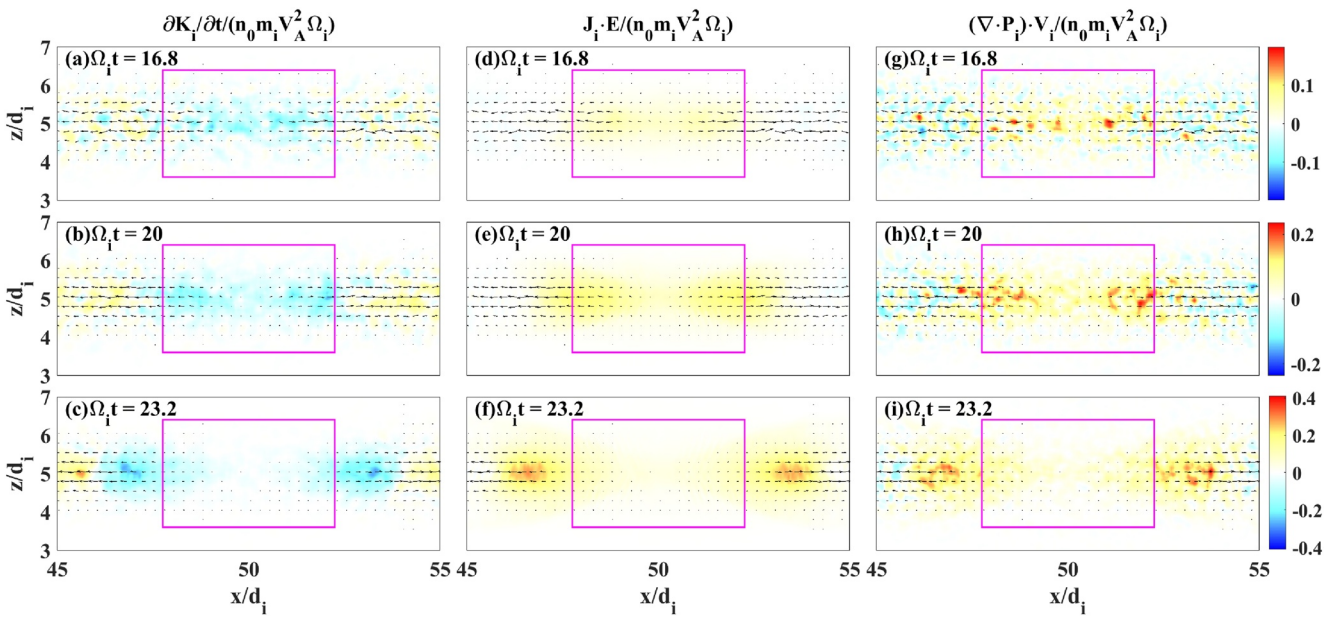

Figure 6. (a–c) Change rate of ion kinetic energy density $\partial K_i/\partial t$, (d–f) work done to ions by electric field $\mathbf{J}_i \cdot \mathbf{E}$, and (g–i) work done by ion pressure gradient force $(\nabla \cdot \overline{\mathbf{P}}_i) \cdot \mathbf{V}_i$ near the reconnection site, shown in colors, with ion bulk kinetic energy flux shown in arrows at $\Omega_i t$ = 16.8, 20.0, and 23.2.

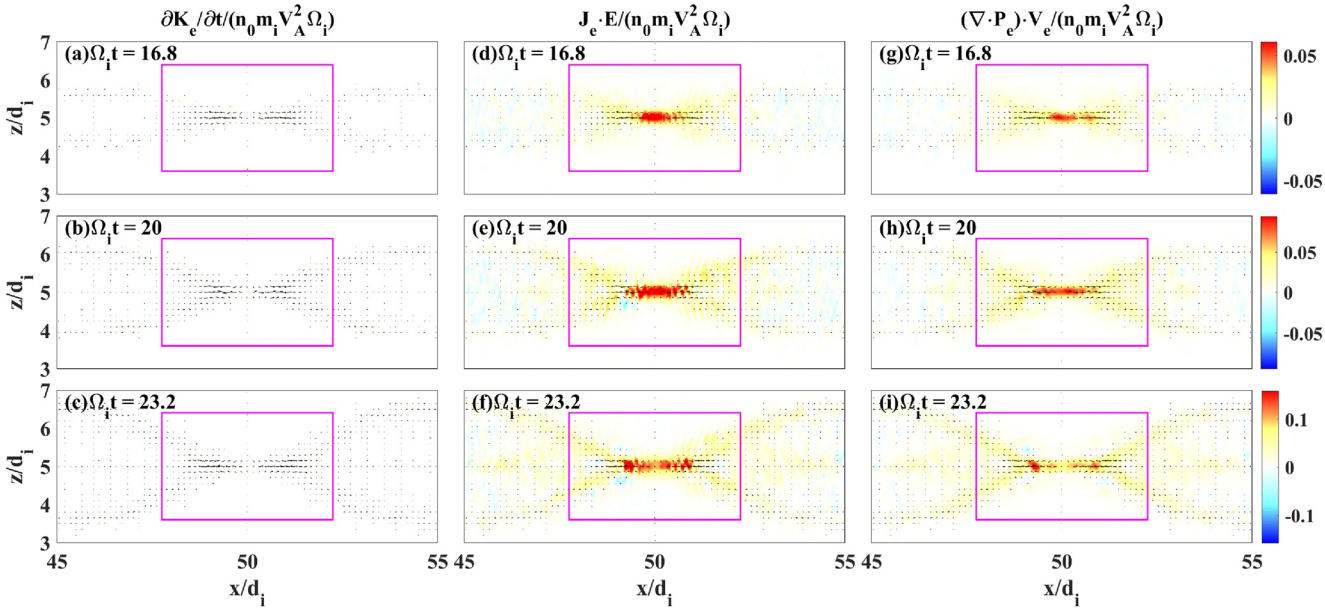

Figure 7. (a–c) Change rate of electron kinetic energy density $\partial K_i/\partial t$, (d–f) work done to electrons by electric field $\mathbf{J}_e \cdot \mathbf{E}$, and (g–i) work done by electron pressure gradient force $(\nabla \cdot \bar{P}_e) \cdot V_e$ near the reconnection site, shown in colors, with electron bulk kinetic energy flux shown in arrows at $\Omega_i t = 16.8$, 20.0, and 23.2.

Table 2 gives us more detailed information on particle kinetic energy conversion, where ions and electrons show great similarity. The local-time change rate of bulk kinetic energy $\partial K_s/\partial t$ equals the outflow of the kinetic flux $\nabla \cdot \left(K_s \mathbf{V}_s\right)$, indicating that both ions and electrons are barely accelerated at the reconnection site. The reason is that the two source terms $-\left(\nabla \cdot \bar{\mathbf{P}}_s\right) \cdot \mathbf{V}_s$ and $\mathbf{J}_s \cdot \mathbf{E}$ compensate each other. Because $\left(\nabla \cdot \bar{\mathbf{P}}_s\right) \cdot \mathbf{V}_s$ is positive and large, according to Equation 3, most of the magnetic energy is converted to thermal energy as shown below.

In Figure 8, the terms in Equation 3 are plotted for ions. As shown in Figures 8d–8f (also in Figures 6g–6i), the source term for the thermal energy gain, $\left(\nabla \cdot \bar{\mathbf{P}}_i\right) \cdot \mathbf{V}_i$, is large and positive at the reconnection site. However, the local thermal energy also descends at the reconnection site ($\partial U_i/\partial t < 0$). Instead, the energy gained from work by ion pressure gradient force, $\left(\nabla \cdot \bar{\mathbf{P}}_i\right) \cdot \mathbf{V}_i$, is converted to ion enthalpy flux ($\mathbf{H}_i$) outflow (the arrows in Figures 8a–8c). The enthalpy flux represents the heated plasma flowing at a bulk velocity. The outflow of the enthalpy flux corresponds to the formation and outflow of the reconnection fronts. As the enthalpy flux propagates downstream, plasmas downstream are heated; therefore, a downstream-positive temperature gradient is formed, leading to the backflow of the ion heat flux $\mathbf{Q}_i$ from downstream to the reconnection site.

Table 2
Integration of Terms in Electron and Ion Kinetic Energy Conversion Equation Near the Reconnection Site

Species	$\Omega_i t$	$\partial K_s/\partial t$	$\nabla \cdot \left(K_s \mathbf{V}_s\right)$	$-\left(\nabla \cdot \bar{\mathbf{P}}_s\right) \cdot \mathbf{V}_s$	$\mathbf{J}_s \cdot \mathbf{E}$
Ion	16.8	−0.155	0.155	−0.202	0.211
	20.0	−0.276	0.290	−0.446	0.459
	23.2	−0.205	0.203	−0.446	0.456
Electron	16.8	0.002	0.0005	−0.062	0.069
	20.0	0.004	0.001	−0.138	0.152
	23.2	0.004	0.005	−0.197	0.233

As shown in Figure 9, the electron thermal energy conversion at the reconnection site resembles the ion thermal energy conversion in many aspects, for instance, the decrease of local thermal energy and the outflow of the electron enthalpy flux. However, the electron heat flux flows out of the reconnection site along the separatrices, unlike the ion heat flux.

We examine the detailed thermal energy budgets at the reconnection site in Table 3. For both ions and electrons, the source term, that is, the work done by the pressure gradient force, $\left(\nabla \cdot \bar{\mathbf{P}}_s\right) \cdot \mathbf{V}_s$, leads to the thermal energy gain. The local thermal energy also decreases, $\partial U_i/\partial t < 0$. As a result, the energy is converted to the outflow of the enthalpy flux $\mathbf{H}_s$. As a secondary effect caused by the temperature gradient, the heat flux $\mathbf{Q}_s$ can be neglected during the process. Since the plasmas downstream become frozen-in with the magnetic field lines, the enthalpy flux propagates with

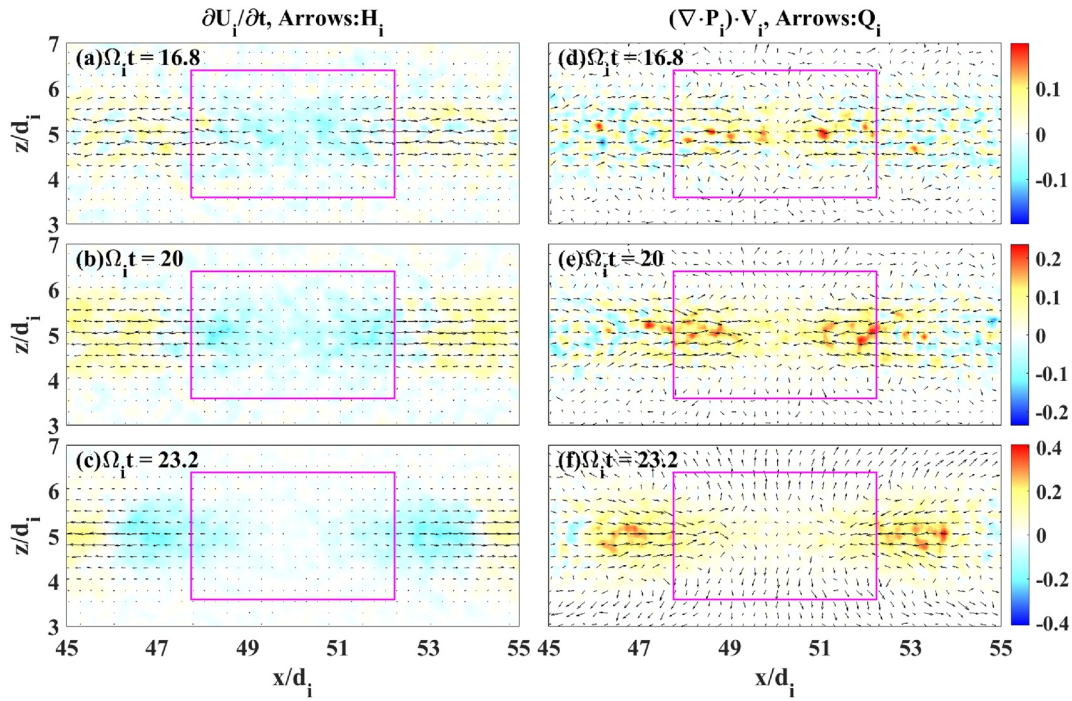

Figure 8. The change rate of ion thermal energy density $\partial U_i/\partial t$ (left) and work done by ion pressure gradient force $\left(\nabla \cdot \overline{\mathbf{P}}_i\right) \cdot \mathbf{V}_i$ (right) near the reconnection site, shown in colors, with ion enthalpy flux $\mathbf{H}_i$ (left) and ion heat flux $\mathbf{Q}_i$ (right) shown in arrows at $\Omega_i t = 16.8, 20.0, 23.2$.

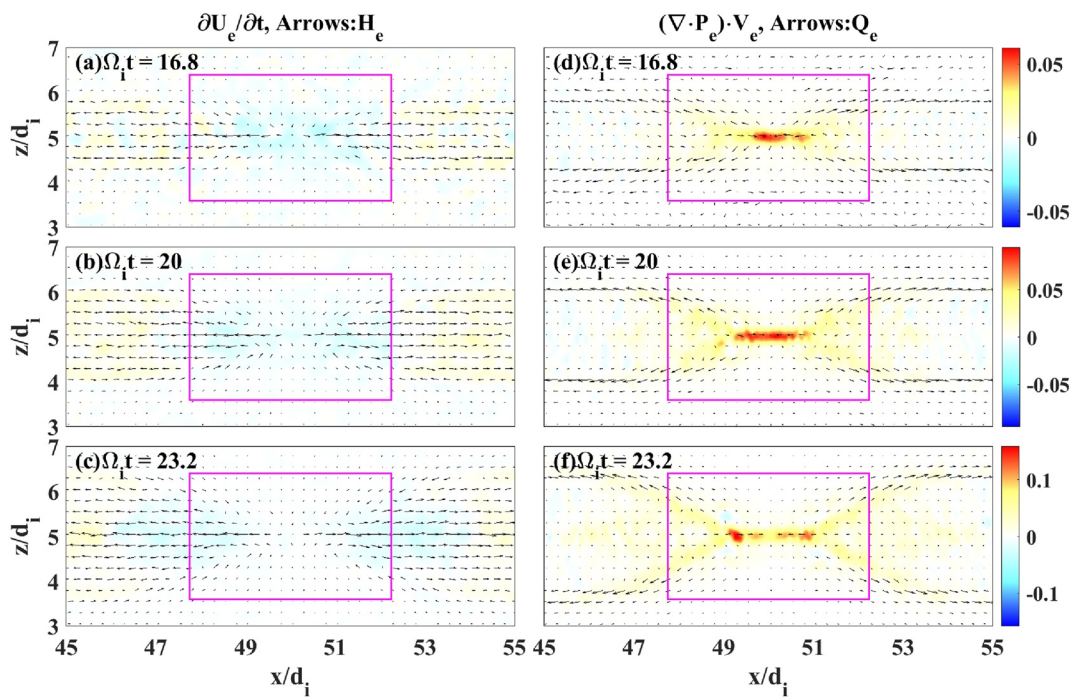

Figure 9. The change rate of electron thermal energy density $\partial U_e/\partial t$ (left) and work done by electron pressure gradient force $\left(\nabla \cdot \overline{\mathbf{P}}_e\right) \cdot \mathbf{V}_e$ (right) near the reconnection site, shown in colors, with electron enthalpy flux $\mathbf{H}_e$ (left) and electron heat flux $\mathbf{Q}_e$ (right) shown in arrows at $\Omega_i t = 16.8, 20.0, 23.2$.

Table 3
Integration of Terms in Electron and Ion Thermal Energy Conversion Equation (Equation 3) Near the Reconnection Site

Species	$\Omega_i t$	$\partial U_s/\partial t$	$\nabla \cdot \mathbf{H}_s$	$\nabla \cdot \mathbf{Q}_s$	$\left(\nabla \cdot \bar{\mathbf{P}}_s\right) \cdot \mathbf{V}_s$
Ion	16.8	−0.201	0.457	−0.106	0.202
	20.0	−0.361	0.884	−0.162	0.446
	23.2	−0.329	0.779	−0.005	0.446
Electron	16.8	−0.029	0.065	0.026	0.062
	20.0	−0.046	0.137	0.037	0.138
	23.2	−0.054	0.188	0.020	0.197

the downstream piling up of magnetic field lines, which are exactly the reconnection fronts we will investigate in the following sections.

3.3. Reconnection Front

The aforementioned outflow of the Poynting flux, enthalpy flux, and bulk kinetic flux from the reconnection site forms the reconnection fronts. During the formation of the reconnection front, $t = 15\Omega_i^{-1} - 28\Omega_i^{-1}$, the frozen-in condition $\mathbf{E} + \mathbf{V} \times \mathbf{B} = 0$ is roughly satisfied at the pileup region, and the motion of the plasma can be described by the momentum equation

$$\rho \mathrm{d}\mathbf{V}/\mathrm{d}t = -\nabla \cdot \bar{\mathbf{P}} + \mathbf{J} \times \mathbf{B} = -\nabla \cdot \left(\bar{\mathbf{P}}_i + \bar{\mathbf{P}}_e\right) + \frac{1}{\mu_0}\left(\mathbf{B} \cdot \nabla\right)\mathbf{B} - \frac{1}{2\mu_0}\nabla B^2. \quad (4)$$

The terms on the right-hand side are ion and electron pressure gradient force, magnetic tension force, and magnetic pressure gradient force, respectively. Figure 10 plots the x-component of these terms (averaged over z from $3.6d_i$ to $6.4d_i$) at the front-forming region. The dominant terms are ion pressure gradient force and magnetic tension force. In the beginning, for example, at $t = 15\Omega_i^{-1}$, the forces are not balanced; the magnetic tension force drags the plasma downstream. The plasmas along with magnetic field lines at the front are accelerated. The ion pressure increases as the plasmas march downstream and encounter the unreconnected current sheet. Finally, those two terms are balanced at about $t = 28\Omega_i^{-1}$. The acceleration of fronts is finished, so that fronts can move at a constant speed afterward.

Once a reconnection front is well developed, it reaches a force balance (Figure 10d) and moves at a constant speed (Figure 3). Therefore, we choose a typical time $\Omega_i t$ =40.0 for illustration. Other times have been researched and present consistent results (not shown in this study).

Considering the moving front, the partial derivative in Equations 2 and 3 should be modified to the material derivative $\mathrm{d}/\mathrm{d}t = \partial/\partial t + \mathbf{V}_s \cdot \nabla$, where $s = i, e$ for ion and electron energy conversion equation, respectively.

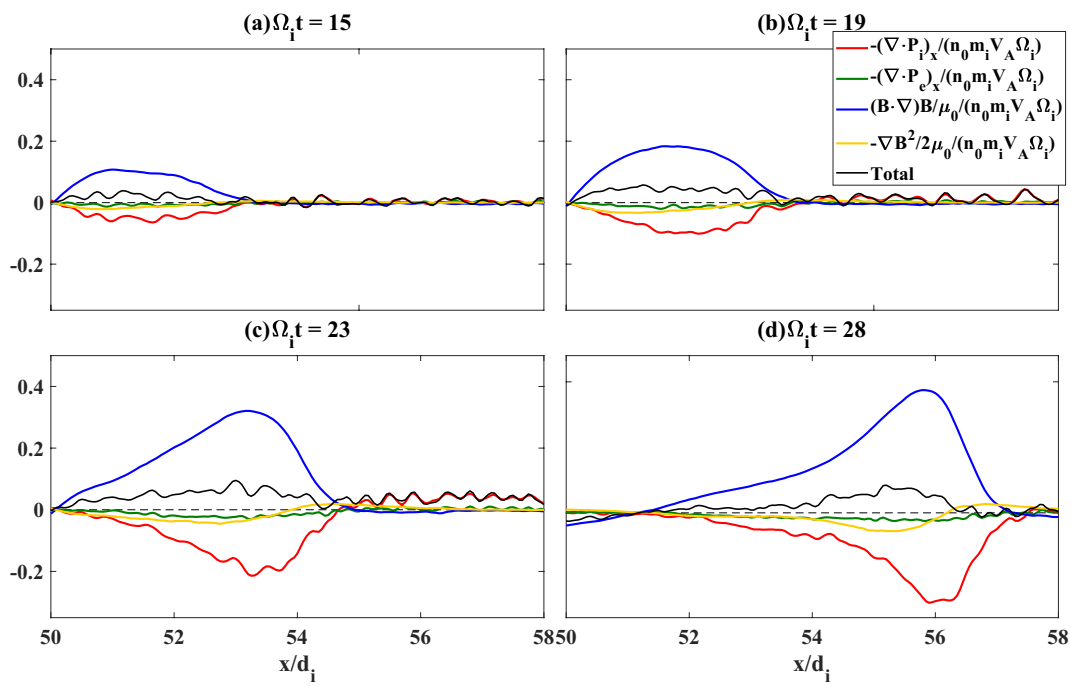

Figure 10. X-components of force terms on the right-hand side of Equation 4, that is, ion pressure gradient force (red), electron pressure gradient force (green), magnetic tension force (blue), and magnetic pressure gradient force (yellow) at $\Omega_i t = 15, 19, 23, 28$. Those terms are averaged over z from $3.6d_i$ to $6.4d_i$ and plotted on the right side of the x-axis.

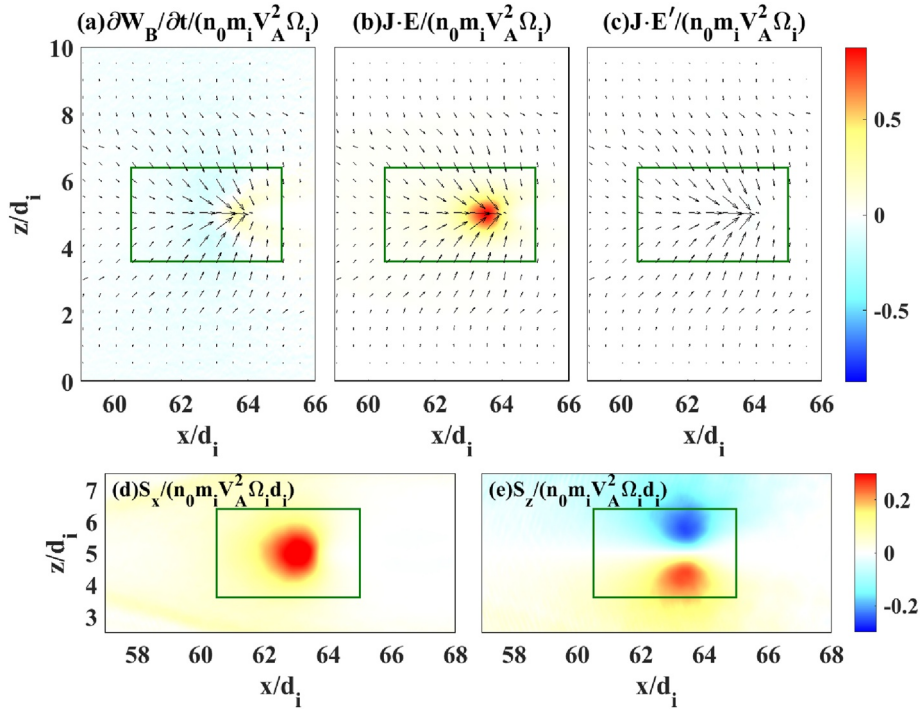

Figure 11. (a) The change rate of magnetic energy density $\partial W_B/\partial t$, (b) work done by electric field E, and (c) $\mathbf{J}\cdot\mathbf{E}'$ near the right-hand-side front at $\Omega_i t = 40.0$. Poynting flux is shown in arrows in (a–c). X-component and z-component of Poynting flux are also plotted in (d and e), respectively.

As for the field energy conversion equation, the velocity is approximated as the front-moving velocity $\mathbf{V}_\mathrm{F}$ downstream along the x-axis: $\mathrm{d}/\mathrm{d}t = \partial/\partial t + \mathbf{V}_\mathrm{F}\cdot\nabla$. Hence, the modified energy conversion equations for moving fronts are:

$$\mathrm{d}W_E/\mathrm{d}t + \mathrm{d}W_B/\mathrm{d}t + \nabla\cdot\mathbf{S} - \mathbf{V}_\mathrm{F}\cdot\nabla\left(W_E + W_B\right) = -\mathbf{J}\cdot\mathbf{E}, \tag{5}$$

$$\mathrm{d}K_s/\mathrm{d}t + K_s\nabla\cdot\mathbf{V}_s = -\left(\nabla\cdot\bar{\mathbf{P}}_s\right)\cdot\mathbf{V}_s + \mathbf{J}_s\cdot\mathbf{E}, \tag{6}$$

$$\mathrm{d}U_s/\mathrm{d}t + U_s\nabla\cdot\mathbf{V}_s + \nabla\cdot\left(\bar{\mathbf{P}}_s\cdot\mathbf{V}_s\right) + \nabla\cdot\mathbf{Q}_s = \left(\nabla\cdot\bar{\mathbf{P}}_s\right)\cdot\mathbf{V}_s, \tag{7}$$

where $\nabla\cdot\mathbf{S} - \mathbf{V}_\mathrm{F}\cdot\nabla\left(W_E + W_B\right)$ in Equation 5 is the actual Poynting flux transported out of the moving front from its boundaries (negative for flow-in), $K_s\nabla\cdot\mathbf{V}_s$ and $U_s\nabla\cdot\mathbf{V}_s$ represent compression and inflation of the plasma at the reconnection front, respectively, and $\bar{\mathbf{P}}_s\cdot\mathbf{V}_s$ is still a part of the enthalpy flux, representing outflow or inflow of heated bulk plasmas.

The terms in the field energy conversion equation, Equation 5, at the moving front are presented in Figure 11. The arrows represent Poynting flux, whose x- and z-components are also plotted in Figures 11d and 11e. The integration (over the green box at the reconnection front) of terms in Equation 5 is listed in Table 4. The total magnetic energy at the moving front hardly changes, $\mathrm{d}W_B/\mathrm{d}t \approx 0$, that is, neither cumulation nor depletion of magnetic energy occurs during this stage. The major energy income at the reconnection front is the inflowing Poynting flux. Surprisingly, the net inflow of the Poynting flux is predominantly S_z from the unreconnected magnetic field (through the upper and lower boundaries of the green box) rather than S_x from the reconnection site (through the left boundary of the green box), suggesting that the energy conversion at fronts becomes unrelated to the reconnection site. The input of Poynting flux is consumed by work done by the electric field, $\mathbf{J}\cdot\mathbf{E}$, and converted to particle kinetic energies. $\mathbf{J}\cdot\mathbf{E}'$ is almost zero since plasmas are frozen-in at the front.

Table 4
Integration of Terms in Field Energy Conversion Equation at the Moving Reconnection Front at $\Omega_i t = 40.0$

$\mathrm{d}W_B/\mathrm{d}t$	$\mathrm{d}W_E/\mathrm{d}t$	$\nabla\cdot\mathbf{S} - \mathbf{V}_\mathrm{F}\cdot\nabla\left(W_B + W_E\right)$	$\mathbf{J}\cdot\mathbf{E}$	$\mathbf{J}\cdot\mathbf{E}'$
0.004	0.001	−1.752	1.729	−0.013

Based on Equation 6, Figure 12 and Table 5 present the kinetic energy conversion of ions and electrons at the front. Both local-time derivatives

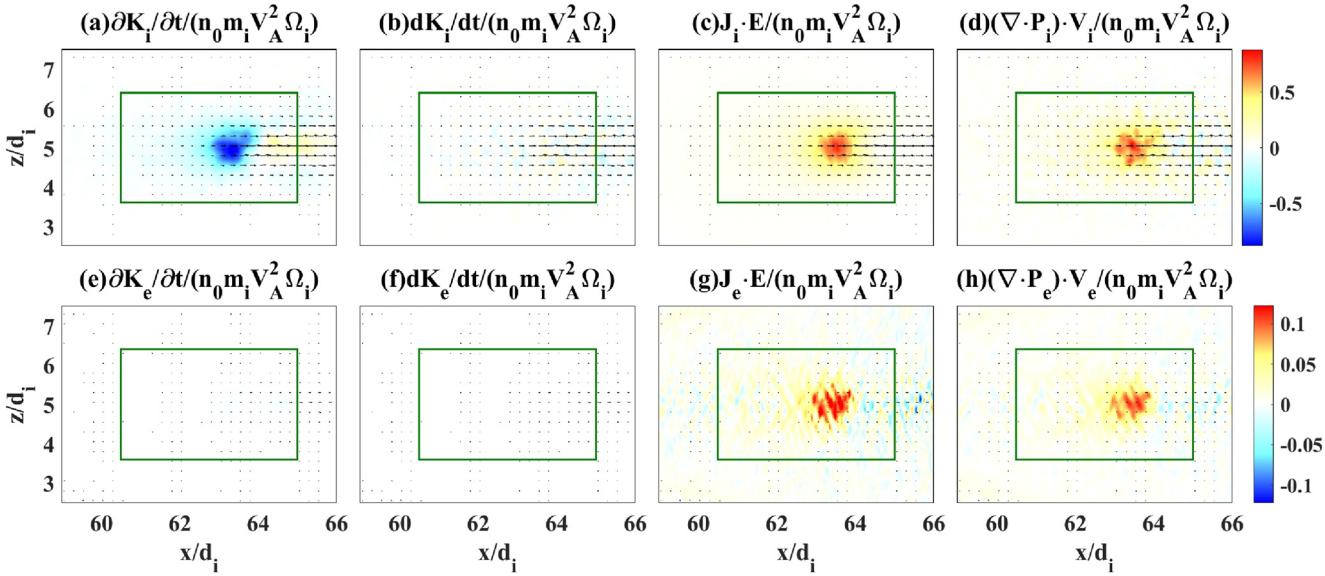

Figure 12. (a, e) Time partial derivative of kinetic energy density, (b, f) material derivative of kinetic energy density, (c, g) work by electric field, and (d, h) work by particle pressure gradient force near the right-hand-side front at $\Omega_i t = 40.0$. Terms of ions are plotted in the upper row, and terms of electrons are plotted in the lower row. Arrows represent the ion bulk kinetic flux (upper row) and the electric bulk kinetic flux (lower row).

and material derivatives are plotted for comparison. Similar to that at the reconnection site, the bulk acceleration of particles is not obvious at the reconnection front ($dK_s/dt \approx 0$). This is because the work done by the electric field $\mathbf{J}_s \cdot \mathbf{E}$ is compensated by the work done by the particle pressure gradient force $\left(\nabla \cdot \overline{\mathbf{P}}_s\right) \cdot \mathbf{V}_s$ (Figures 12c, 12d, 12g, and 12h and the last two columns of Table 5). The electron bulk kinetic energy flux concentrates at the separatrices near the X-line, where the electrons are mostly accelerated. Therefore, the electron bulk kinetic energy flux at the front appears relatively small. The effect of compression and inflation of the plasmas $K_s \nabla \cdot \mathbf{V}_s$ at the front is negligible (see the third column in Table 5), which verifies that the area of the front is steady during the moving phase.

The ion and electron thermal energy budgets are examined by analyzing Equation 7. As shown in Figure 13 and Table 6, the work by ion and electron pressure gradient force $\left(\nabla \cdot \overline{\mathbf{P}}_s\right) \cdot \mathbf{V}_s$ mainly turns into the enthalpy flux (more specifically, $\overline{\mathbf{P}}_s \cdot \mathbf{V}_s$ flux) at the reconnection front. Locally heated ions and electrons account for a small proportion. The contribution of the heat flux $\mathbf{Q}_s$ is also insignificant. The outflow of $\overline{\mathbf{P}}_s \cdot \mathbf{V}_s$ flux suggests that the bulk velocity of the plasmas ahead of the front is slightly faster than the constant front-moving velocity $\mathbf{V}_F$. This is because the ions ahead of the front can be reflected and accelerated, forming a jet downstream, that is, the precursor flow (S. Lu et al., 2016; X. Z. Zhou et al., 2010, 2011).

4. Conclusions and Discussions

In this study, we use a 2D PIC simulation to analyze the energy conversion from magnetic energy to particle kinetic energies at magnetic reconnection site and reconnection front. Our main conclusions are summarized below:

1. The reconnection rate is insufficient to reflect the energy conversion rate of transient magnetic reconnection. This is because the reconnection rate merely represents the energy conversion near the reconnection site, which accounts for a small fraction of the energy conversion.
2. Energy conversion mainly occurs at the reconnection fronts instead of the reconnection site. On one hand, the duration of energy conversion at the fronts lasts much longer than near the reconnection site. On the other hand, the electric field grows exponentially at the fronts; therefore, energy conversion rate $\mathbf{J} \cdot \mathbf{E}$, especially $\mathbf{J}_i \cdot \mathbf{E}$ is enhanced at the fronts.

Table 5
Integration of Terms in Ion and Electron Bulk Kinetic Energy Conversion Equations at the Moving Reconnection Front at $\Omega_i t = 40.0$

Species	dK_s/dt	$K_s \nabla \cdot \mathbf{V}_s$	$-\left(\nabla \cdot \overline{\mathbf{P}}_s\right) \cdot \mathbf{V}_s$	$\mathbf{J}_s \cdot \mathbf{E}$
Ion	0.024	−0.010	−1.501	1.543
Electron	0.004	−0.0001	−0.165	0.185

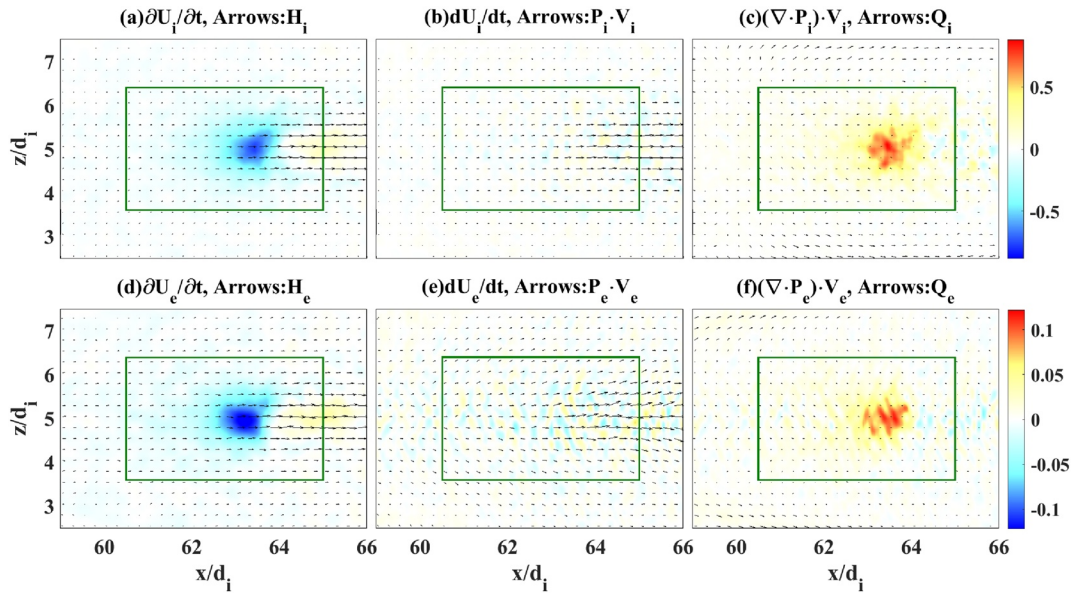

Figure 13. (a, d) Time partial derivative of thermal energy density, (b, e) material derivative of thermal energy density, and (c, f) work by particle pressure gradient force near the right-hand side front at $\Omega_i t = 40.0$. Arrows represent (a, d) the enthalpy flux, (b, e) $\bar{P}_i \cdot V_i$ flux, and (c, f) heat flux. Terms of ions are plotted in the upper row, and terms of electrons are plotted in the lower row.

3. At the beginning of the reconnection, the Poynting flux is driven into the reconnection site from its top and bottom boundaries. Part of the inflow and the local magnetic field energy are mainly converted to the downstream enthalpy flux through the work done by the electric field. The remaining Poynting flux and local bulk kinetic are diverted to the outflow from the left and right boundaries, along with the enthalpy flux, forming the reconnection front. The cause is the magnetic tension force not being fully compensated by the thermal pressure gradient. Therefore, the reconnection site serves as a trigger to provide reconnected magnetic flux and generate the reconnection fronts.
4. At the well-developed front, energy conversion is unrelated to the reconnection site, with neither magnetic energy nor kinetic energy income from the X-line. Nevertheless, the Poynting flux flows in from the top and bottom of the front and is converted through work by the electric field to particle energy in the form of $\bar{\mathbf{P}} \cdot \mathbf{V}$ flux flowing away from the front (even in the material frame). Compared to the $\bar{\mathbf{P}} \cdot \mathbf{V}$ flux, the local particle bulk acceleration and heating are much less significant.

Our research shows that the reconnection fronts account for more than 60% of the total energy conversion in unsteady magnetic reconnection, supporting the claim that the energy conversion predominantly occurs at reconnection fronts (Angelopoulos et al., 2013; Khotyaintsev et al., 2017; Sitnov et al., 2009; Yi et al., 2019). Former simulations also found that magnetic energy conversion favors ions more than electrons (Goldman et al., 2015; Sitnov et al., 2009), and particles are more inclined to be heated than accelerated (Aunai et al., 2011; S. Lu, Lu, Huang, & Wang, 2013). Through PIC simulations, Song et al. (2020) found that the reconnection front is accelerated by the magnetic curvature force and hindered by the pressure gradient force. They also studied how magnetic energy contributes to plasma heating and acceleration in the developing reconnection front. These conclusions are consistent with ours. For the first time, we studied the connection between the reconnection site and the reconnection fronts in terms of energy conversion, claiming that formation of the reconnection fronts requires energy (Poynting flux, bulk kinetic energy flux, and enthalpy flux) from the reconnection site. We also investigated at a later period when the reconnection front maintains a constant speed downstream, the time derivative terms reduce to almost zero. It is concluded that energy conversion at the well-developed front is unrelated to the reconnection site, whose energy source is the local Poyn-

Table 6
Integration of Terms in Ion and Electron Thermal Energy Conversion Equations at the Moving Reconnection Front at $\Omega_i t = 40.0$

Species	dU_s/dt	$U_s \nabla \cdot \mathbf{V}_s$	$\nabla \cdot \left(\bar{\mathbf{P}}_s \cdot \mathbf{V}_s\right)$	$\nabla \cdot \mathbf{Q}_s$	$\left(\nabla \cdot \bar{\mathbf{P}}_s\right) \cdot \mathbf{V}_s$
Ion	0.025	−0.016	1.489	−0.037	1.501
Electron	0.001	−0.003	0.157	−0.037	0.165

ting flux in z-direction. Experiments on MRX suggested that 2/3 of the dissipated magnetic energy is transferred to ions and 1/3 to electrons (Yamada et al., 2014). In our simulation, energy gained by ions accounts for 60%, and 40% for electrons at the reconnection site. While at the reconnection fronts, the proportion of ions grows to 89%. The plasmas in the MRX facility span several ion inertial lengths, which are identical to the situation near the reconnection site.

We have shown that fronts play a vital role in energy conversion. It is intriguing to think about the condition when characteristic size is small enough that it fails to form a steadily moving front, for instance, electron-only reconnection, and reconnection with multiple ion-scale or sub-ion-scale magnetic islands. Furthermore, the effects of a guide field are not considered here; it is known that the guide field will introduce asymmetric in reconnection configuration and suppress the growth of the reconnection electric field. It is worthwhile to investigate the effects of a guide field on energy conversion. The 3D simulations have shown that structures in the y-direction at the reconnection fronts emerge load and generator regions (Khotyaintsev et al., 2017; Lapenta et al., 2014; Vapirev et al., 2013). Therefore, the contribution from the 3D effects, especially the k_y structures, to the overall energy conversion needs further studies.

Data Availability Statement

The simulation results described in Section 3 are generated from our computer simulation model. Moreover, the simulation model is described in Section 2. The simulation data for the figures and tables in the study can be downloaded from https://dx.doi.org/10.12176/01.99.00682.

Acknowledgments
This work was supported by the Strategic Priority Research Program of Chinese Academy of Sciences, Grant No. XDB 41000000, the NSFC grant 41774169. Grateful acknowledgment is made to the data resources from "National Space Science Data Center, National Science & Technology Infrastructure of China (http://www.nssdc.ac.cn)."

References

Angelopoulos, V., Runov, A., Zhou, X. Z., Turner, D. L., Kiehas, S. A., Li, S. S., & Shinohara, I. (2013). Electromagnetic energy conversion at reconnection fronts. *Science*, *341*(6153), 1478–1482. https://doi.org/10.1126/science.1236992

Aunai, N., Belmont, G., & Smets, R. (2011). Energy budgets in collisionless magnetic reconnection: Ion heating and bulk acceleration. *Physics of Plasmas*, *18*(12), 122901. https://doi.org/10.1063/1.3664320

Baker, D. N., Pulkkinen, T. I., Angelopoulos, V., Baumjohann, W., & McPherron, R. L. (1996). Neutral line model of substorms: Past results and present view. *Journal of Geophysical Research*, *101*(A6), 12975–13010. https://doi.org/10.1029/95JA03753

Birn, J., & Hesse, M. (2005). Energy release and conversion by reconnection in the magnetotail. *Annales Geophysicae*, *23*(10), 3365–3373. https://doi.org/10.5194/angeo-23-3365-2005

Birn, J., & Hesse, M. (2010). Energy release and transfer in guide field reconnection. *Physics of Plasmas*, *17*(1), 1–11. https://doi.org/10.1063/1.3299388

Birn, J., & Priest, E. R. (2007). *Reconnection of magnetic fields*. Cambridge University Press. https://doi.org/10.1086/171911

Deng, X., Ashour-Abdalla, M., Zhou, M., Walker, R., El-Alaoui, M., Angelopoulos, V., et al. (2010). Wave and particle characteristics of earthward electron injections associated with dipolarization fronts. *Journal of Geophysical Research*, *115*(9), 1–14. https://doi.org/10.1029/2009JA015107

Divin, A., Khotyaintsev, Y. V., Vaivads, A., André, M., Markidis, S., & Lapenta, G. (2015). Evolution of the lower hybrid drift instability at reconnection jet front. *Journal of Geophysical Research: Space Physics*, *120*(4), 2675–2690. https://doi.org/10.1002/2014JA020503

Eastwood, J. P., Phan, T. D., Drake, J. F., Shay, M. A., Borg, A. L., Lavraud, B., & Taylor, M. G. G. T. (2013). Energy partition in magnetic reconnection in Earth's magnetotail. *Physical Review Letters*, *110*(22), 1–5. https://doi.org/10.1103/PhysRevLett.110.225001

Fu, H. S., Cao, J. B., Khotyaintsev, Y. V., Sitnov, M. I., Runov, A., Fu, S. Y., et al. (2013). Dipolarization fronts as a consequence of transient reconnection: In situ evidence. *Geophysical Research Letters*, *40*(23), 6023–6027. https://doi.org/10.1002/2013GL058620

Fu, X. R., Lu, Q. M., & Wang, S. (2006). The process of electron acceleration during collisionless magnetic reconnection. *Physics of Plasmas*, *13*(1), 1–7. https://doi.org/10.1063/1.2164808

Goldman, M. V., Newman, D. L., & Lapenta, G. (2015). What can we learn about magnetotail reconnection from 2D PIC Harris-Sheet simulations? *Space Science Reviews*, *199*(1–4), 651–688. https://doi.org/10.1007/s11214-015-0154-y

Huang, C., Lu, Q., & Wang, S. (2010). The mechanisms of electron acceleration in antiparallel and guide field magnetic reconnection. *Physics of Plasmas*, *17*(7), 072306. https://doi.org/10.1063/1.3457930

Huang, C., Wu, M., Lu, Q., Wang, R., & Wang, S. (2015). Electron acceleration in the dipolarization front driven by magnetic reconnection. *Journal of Geophysical Research: Space Physics*, *120*(3), 1759–1765. https://doi.org/10.1002/2014JA020918

Kepko, L., McPherron, R. L., Amm, O., Apatenkov, S., Baumjohann, W., Birn, J., et al. (2015). Substorm current wedge revisited. *Space Science Reviews*, *190*(1–4). https://doi.org/10.1007/s11214-014-0124-9

Khotyaintsev, Y. V., Divin, A., Vaivads, A., André, M., & Markidis, S. (2017). Energy conversion at dipolarization fronts. *Geophysical Research Letters*, *44*(3), 1234–1242. https://doi.org/10.1002/2016GL071909

Lapenta, G., Goldman, M. V., Newman, D. L., Markidis, S., & Divin, A. (2014). Electromagnetic energy conversion in downstream fronts from three dimensional kinetic reconnection. *Physics of Plasmas*, *21*(5), 055702. https://doi.org/10.1063/1.4872028

Lin, J., & Forbes, T. G. (2000). Effects of reconnection on the coronal mass ejection process. *Journal of Geophysical Research*, *105*(A2), 2375–2392. https://doi.org/10.1029/1999ja900477

Liu, C. M., Fu, H. S., Vaivads, A., Khotyaintsev, Y. V., Gershman, D. J., Hwang, K. J., et al. (2018). Electron jet detected by MMS at dipolarization front. *Geophysical Research Letters*, *45*(2), 556–564. https://doi.org/10.1002/2017GL076509

Liu, C. M., Fu, H. S., Xu, Y., Khotyaintsev, Y. V., Burch, J. L., Ergun, R. E., et al. (2018). Electron-scale measurements of dipolarization front. *Geophysical Research Letters*, *45*(10), 4628–4638. https://doi.org/10.1029/2018GL077928

Liu, J., Angelopoulos, V., Zhou, X.-Z., & Runov, A. (2014). Magnetic flux transport by dipolarizing flux bundles. *Journal of Geophysical Research: Space Physics*, *119*(2), 909–926. https://doi.org/10.1002/2013JA019395

Lu, Q., Huang, C., Xie, J., Wang, R., Wu, M., Vaivads, A., & Wang, S. (2010). Features of separatrix regions in magnetic reconnection: Comparison of 2-D particle-in-cell simulations and Cluster observations. *Journal of Geophysical Research*, *115*(11), 1–7. https://doi.org/10.1029/2010JA015713

Lu, Q., Lu, S., Huang, C., Wu, M., & Wang, S. (2013). Self-reinforcing process of the reconnection electric field in the electron diffusion region and onset of collisionless magnetic reconnection. *Plasma Physics and Controlled Fusion*, *55*(8), 085019. https://doi.org/10.1088/0741-3335/55/8/085019

Lu, S., Angelopoulos, V., & Fu, H. (2016). Suprathermal particle energization in dipolarization fronts: Particle-in-cell simulations. *Journal of Geophysical Research: Space Physics*, *121*(10), 9483–9500. https://doi.org/10.1002/2016JA022815

Lu, S., Lu, Q., Huang, C., & Wang, S. (2013). The transfer between electron bulk kinetic energy and thermal energy in collisionless magnetic reconnection. *Physics of Plasmas*, *20*(6), 061203. https://doi.org/10.1063/1.4811119

Lu, S., Lu, Q., Lin, Y., Wang, X., Ge, Y., Wang, R., et al. (2015). Dipolarization fronts as earthward propagating flux ropes: A three-dimensional global hybrid simulation. *Journal of Geophysical Research: Space Physics*, *120*(8), 6286–6300. https://doi.org/10.1002/2015JA021213

Lu, S., Wang, R., Lu, Q., Angelopoulos, V., Nakamura, R., Artemyev, A. V., et al. (2020). Magnetotail reconnection onset caused by electron kinetics with a strong external driver. *Nature Communications*, *11*(1), 1–7. https://doi.org/10.1038/s41467-020-18787-w

Masuda, S., Kosugi, T., Hara, H., Tsuneta, S., & Ogawara, Y. (1994). A loop-top hard X-ray source in a compact solar flare as evidence for magnetic reconnection. *Nature*, *371*(6497), 495–497. https://doi.org/10.1038/371495a0

Runov, A., Angelopoulos, V., Sitnov, M. I., Sergeev, V. A., Bonnell, J., McFadden, J. P., et al. (2009). THEMIS observations of an earthward-propagating dipolarization front. *Geophysical Research Letters*, *36*(14), 1–7. https://doi.org/10.1029/2009GL038980

Shay, M. A., Haggerty, C. C., Phan, T. D., Drake, J. F., Cassak, P. A., Wu, P., et al. (2014). Electron heating during magnetic reconnection: A simulation scaling study. *Physics of Plasmas*, *21*(12), 1–11. https://doi.org/10.1063/1.4904203

Sitnov, M. I., Swisdak, M., & Divin, A. V. (2009). Dipolarization fronts as a signature of transient reconnection in the magnetotail. *Journal of Geophysical Research*, *114*(A4). https://doi.org/10.1029/2008ja013980

Song, L., Zhou, M., Yi, Y., Deng, X., Zhong, Z., & Man, H. (2020). Force and energy balance of the dipolarization front. *Journal of Geophysical Research: Space Physics*, *125*(9), 1–11. https://doi.org/10.1029/2020JA028278

Vapirev, A. E., Lapenta, G., Divin, A., Markidis, S., Henri, P., Goldman, M., & Newman, D. (2013). Formation of a transient front structure near reconnection point in 3-D PIC simulations. *Journal of Geophysical Research: Space Physics*, *118*(4), 1435–1449. https://doi.org/10.1002/jgra.50136

Wang, L., Huang, C., Cao, X., Du, A., & Ge, Y. S. (2020). Magnetic energy conversion and transport in the terrestrial magnetotail due to dipolarization fronts. *Journal of Geophysical Research: Space Physics*, *125*(10), 1–11. https://doi.org/10.1029/2020JA028568

Wu, M., Lu, Q., Volwerk, M., Vörös, Z., Zhang, T., Shan, L., & Huang, C. (2013). A statistical study of electron acceleration behind the dipolarization fronts in the magnetotail. *Journal of Geophysical Research: Space Physics*, *118*(8), 4804–4810. https://doi.org/10.1002/jgra.50456

Xu, Y., Fu, H. S., Norgren, C., Hwang, K. J., & Liu, C. M. (2018). Formation of dipolarization fronts after current sheet thinning. *Physics of Plasmas*, *25*(7), 072123. https://doi.org/10.1063/1.5030200

Yamada, M., Kulsrud, R., & Ji, H. (2010). Magnetic reconnection. *Reviews of Modern Physics*, *82*(1), 603–664. https://doi.org/10.1103/RevModPhys.82.603

Yamada, M., Levinton, F. M., Pomphrey, N., Budny, R., Manickam, J., & Nagayama, Y. (1994). Investigation of magnetic reconnection during a sawtooth crash in a high-temperature tokamak plasma. *Physics of Plasmas*, *1*(10), 3269–3276. https://doi.org/10.1063/1.870479

Yamada, M., Yoo, J., Jara-Almonte, J., Daughton, W., Ji, H., Kulsrud, R. M., & Myers, C. E. (2015). Study of energy conversion and partitioning in the magnetic reconnection layer of a laboratory plasma. *Physics of Plasmas*, *22*(5), 056501. https://doi.org/10.1063/1.4920960

Yamada, M., Yoo, J., Jara-Almonte, J., Ji, H., Kulsrud, R. M., & Myers, C. E. (2014). Conversion of magnetic energy in the magnetic reconnection layer of a laboratory plasma. *Nature Communications*, *5*(May). https://doi.org/10.1038/ncomms5774

Yao, Z. H., Rae, I. J., Guo, R. L., Fazakerley, A. N., Owen, C. J., Nakamura, R., et al. (2017). A direct examination of the dynamics of dipolarization fronts using MMS. *Journal of Geophysical Research: Space Physics*, *122*(4), 4335–4347. https://doi.org/10.1002/2016JA023401

Yi, Y., Zhou, M., Song, L., & Deng, X. (2019). On the energy conversion rate during collisionless magnetic reconnection. *The Astrophysical Journal*, *883*(1), L22. https://doi.org/10.3847/2041-8213/ab40c1

Zhong, Z. H., Deng, X. H., Zhou, M., Ma, W. Q., Tang, R. X., Khotyaintsev, Y. V., et al. (2019). Energy conversion and dissipation at dipolarization fronts: A statistical overview. *Geophysical Research Letters*, *46*(22), 12693–12701. https://doi.org/10.1029/2019GL085409

Zhou, M., Ashour-Abdalla, M., Deng, X., Schriver, D., El-Alaoui, M., & Pang, Y. (2009). THEMIS observation of multiple dipolarization fronts and associated wave characteristics in the near-Earth magnetotail. *Geophysical Research Letters*, *36*(20), 4–9. https://doi.org/10.1029/2009GL040663

Zhou, M., Deng, X. H., Zhong, Z. H., Pang, Y., Tang, R. X., El-Alaoui, M., et al. (2019). Observations of an electron diffusion region in symmetric reconnection with weak guide field. *The Astrophysical Journal*, *870*(1), 34. https://doi.org/10.3847/1538-4357/aaf16f

Zhou, X. Z., Angelopoulos, V., Sergeev, V. A., & Runov, A. (2010). Accelerated ions ahead of earthward propagating dipolarization fronts. *Journal of Geophysical Research*, *115*(9), 1–8. https://doi.org/10.1029/2010JA015481

Zhou, X. Z., Angelopoulos, V., Sergeev, V. A., & Runov, A. (2011). On the nature of precursor flows upstream of advancing dipolarization fronts. *Journal of Geophysical Research*, *116*(3), 1–8. https://doi.org/10.1029/2010JA016165